Optics Letters

Topology optimization of multi-track ring resonators and 2D microcavities for nonlinear frequency conversion

Zin Lin,[1] Marko Lončar,[1] and Alejandro W. Rodriguez[2,*]

[1]John A. Paulson School of Engineering and Applied Sciences, Harvard University, Cambridge, Massachusetts 02138, USA
[2]Department of Electrical Engineering, Princeton University, Princeton, New Jersey 08544, USA
*Corresponding author: arod@princeton.edu

Received 14 April 2017; revised 3 June 2017; accepted 23 June 2017; posted 23 June 2017 (Doc. ID 290663); published 13 July 2017

We exploit recently developed topology-optimization techniques to design complex, wavelength-scale resonators for enhancing various nonlinear $\chi^{(2)}$ and $\chi^{(3)}$ frequency conversion processes. In particular, we demonstrate aperiodic, multi-track ring resonators and two-dimensional slab microcavities exhibiting long lifetimes $Q \gtrsim 10^4$, small modal volumes $V \gtrsim (\lambda/2n)^3$, and among the largest nonlinear overlaps (a generalization of phase matching in large-etalon waveguides) possible, paving the way for efficient, compact, and wide-bandwdith integrated nonlinear devices.

OCIS codes: (190.0190) Nonlinear optics; (050.1755) Computational electromagnetic methods.

https://doi.org/10.1364/OL.42.002818

Nonlinear frequency conversion (NFC) plays a crucial role in many photonic applications, including ultrashort pulse shaping [1,2], spectroscopy [3], generating novel states of light [4,5], and quantum information processing [6]. A well-known approach for lowering the power requirements of such nonlinear devices is employing optical resonators that confine light for long times (dimensionless quality factors or lifetimes Q) in small volumes V [7–14]. Although microcavity resonators designed for on-chip, infrared applications promise some of the smallest confinement factors available, their implementation is highly limited by the difficult task of identifying wavelength-scale ($V \sim \lambda^3$) structures supporting long-lived, resonant modes at widely separated wavelengths and satisfying rigid frequency matching and mode overlap constraints [15,16]. Recently, we proposed a computational framework based on large-scale topology-optimization (TO) techniques that enables the automatic discovery of multilayer and grating structures exhibiting some of the largest second-harmonic generation (SHG) figures of merit ever predicted [17].

In this Letter, we extend our TO formulation to allow the possibility of more sophisticated nonlinear processes and apply it to the problem of designing rotationally symmetric and slab microresonators that exhibit high-efficiency SHG and sum frequency generation/difference frequency generation (SFG/DFG). In particular, we demonstrate multi-track ring resonators and proof-of-principle two-dimensional (2D) slab cavities supporting multiple, resonant modes (even several octaves apart) that would be impossible to design "by hand." Our designs ensure frequency matching, long radiative lifetimes, and small (wavelength-scale) modal confinement, while simultaneously maximizing the nonlinear modal overlap (or "phase matching") necessary for efficient NFC. For instance, we discover topology-optimized concentric ring cavities exhibiting SHG efficiencies as high as $P_2/P_1^2 = 1.3 \times 10^{25}(\chi^{(2)})^2$ [W^{-1}], even with low operational $Q \sim 10^4$, a performance that is on par with recently fabricated 60 μm diameter, ultrahigh $Q \sim 10^6$ aluminum nitride (AlN) microring resonators [14] ($P_2/P_1^2 \sim 1.13 \times 10^{24}(\chi^{(2)})^2$ [W^{-1}]); essentially, our topology-optimized cavities not only possess the smallest possible modal volumes $\sim(\lambda/n)^3$, but can also operate over wider bandwidths by virtue of their increased nonlinear modal overlap. As reviewed in Refs. [17–19], a typical topology-optimization problem seeks to maximize or minimize an objective function f, subject to certain constraints g, over a set of free variables or degrees of freedom (DOF):

$$\max / \min\ f(\bar{\epsilon}_\alpha), \tag{1}$$

$$g(\bar{\epsilon}_\alpha) \le 0, \tag{2}$$

$$0 \le \bar{\epsilon}_\alpha \le 1, \tag{3}$$

where the DOFs are the normalized dielectric constants $\bar{\epsilon}_\alpha \in [0, 1]$ assigned to each pixel or voxel (indexed α) in a specified volume. The subscript α denotes appropriate spatial discretization $\mathbf{r} \to (i, j, k)_\alpha \Delta$ with respect to Cartesian or curvilinear coordinates. Depending on the choice of background and structural materials, $\bar{\epsilon}_\alpha$ is mapped onto a position-dependent dielectric constant via $\epsilon_\alpha = (\epsilon - \epsilon_{\mathrm{bg}})\bar{\epsilon}_\alpha + \epsilon_{\mathrm{bg}}$. The binarity of the optimized structure is enforced by penalizing the intermediate values $\bar{\epsilon} \in (0, 1)$ or utilizing a variety of filter and regularization methods [18]. Starting from a random initial guess or completely uniform space, the technique discovers complex structures automatically with the aid of powerful gradient-based algorithms such as the method of moving asymptotes (MMA) [20]. For an electromagnetic problem, f and g are typically functions of the electric $\mathbf{E}$

or magnetic $\mathbf{H}$ fields integrated over some region which, in turn, are solutions to Maxwell's equations under some incident current or field. In what follows, we exploit a direct solution of Maxwell's equations:

$$\Delta \times \frac{1}{\mu}\nabla \times \mathbf{E} - \epsilon(\mathbf{r})\omega^2\mathbf{E} = i\omega\mathbf{J}, \tag{4}$$

describing the steady-state $\mathbf{E}(\mathbf{r};\omega)$ in response to incident currents $\mathbf{J}(\mathbf{r},\omega)$ at frequency ω. While the solution of Eq. (4) is straightforward and commonplace, the key to making optimization problems tractable is to obtain a fast-converging and computationally efficient adjoint formulation of the problem [18]. Within the scope of TO, this requires efficient calculations of the derivatives $\frac{\partial f}{\partial \bar{\epsilon}_\alpha}, \frac{\partial g}{\partial \bar{\epsilon}_\alpha}$ at every pixel α, which we perform by exploiting the adjoint variable method (AVM) [18].

Any NFC process can be viewed as a frequency mixing scheme in which two or more *constituent* photons at a set of frequencies $\{\omega_n\}$ interact to produce an output photon at frequency $\Omega = \sum_n c_n\omega_n$, where $\{c_n\}$ can be either negative or positive, depending on whether the corresponding photons are created or destroyed in the process [21]. Given an appropriate nonlinear tensor component $\chi_{ijk\ldots}$, with $i, j, k, \ldots \in \{x, y, z\}$, mediating an interaction between the polarization components $E_i(\Omega)$ and E_{1j}, E_{2k}, …, we begin with a collection of point dipole currents, each at the *constituent* frequency $\omega_n, n \in \{1, 2, \ldots\}$, such that $\mathbf{J}_n = \hat{\mathbf{e}}_{n\nu}\delta(\mathbf{r} - \mathbf{r}')$, where $\hat{\mathbf{e}}_{n\nu} \in \{\hat{\mathbf{e}}_{1j}, \hat{\mathbf{e}}_{2k}, \ldots\}$ is a polarization vector chosen so as to excite the desired electric-field polarization components (ν) of the corresponding mode at an appropriate position $\mathbf{r}'$. Given the choice of incident currents $\mathbf{J}_n$, we solve Maxwell's equations to obtain the corresponding *constituent* electric-field response $\mathbf{E}_n$, from which one can construct a nonlinear polarization current $\mathbf{J}(\Omega) = \bar{\epsilon}(\mathbf{r})\prod_n E_{n\nu}^{|c_n|(*)}\hat{\mathbf{e}}_i$, where $E_{n\nu} = \mathbf{E}_n \cdot \hat{\mathbf{e}}_{n\nu}$ and $\mathbf{J}(\Omega)$ can be generally polarized ($\hat{\mathbf{e}}_i$) in a (chosen) direction that differs from the constituent polarizations $\hat{\mathbf{e}}_{n\nu}$. Here, (*) denotes complex conjugation for negative c_n and no conjugation otherwise. Finally, maximizing the radiated power, $-\mathrm{Re}[\int \mathbf{J}(\Omega)^* \cdot \mathbf{E}(\Omega)\mathrm{d}\mathbf{r}]$, due to $\mathbf{J}(\Omega)$, one is immediately led to the following nonlinear topology-optimization (NLTO) problem:

$$\max_{\bar{\epsilon}} f(\bar{\epsilon};\omega_n) = -\mathrm{Re}\left[\int \mathbf{J}(\Omega)^* \cdot \mathbf{E}(\Omega)\mathrm{d}\mathbf{r}\right], \tag{5}$$

$$\mathcal{M}(\bar{\epsilon},\omega_n)\mathbf{E}_n = i\omega_n\mathbf{J}_n, \qquad \mathbf{J}_n = \hat{\mathbf{e}}_{n\nu}\delta(\mathbf{r} - \mathbf{r}'),$$

$$\mathcal{M}(\bar{\epsilon},\Omega)\mathbf{E}(\Omega) = i\Omega\mathbf{J}(\Omega), \qquad \mathbf{J}(\Omega) = \bar{\epsilon}\prod_n E_{n\nu}^{|c_n|(*)}\hat{\mathbf{e}}_i,$$

$$\mathcal{M}(\bar{\epsilon},\omega) = \nabla \times \frac{1}{\mu}\nabla \times -\epsilon(\mathbf{r})\omega^2,$$

$$\epsilon(\mathbf{r}) = \epsilon_\mathrm{m} + \bar{\epsilon}(\epsilon_\mathrm{d} - \epsilon_\mathrm{m}), \qquad \bar{\epsilon} \in [0, 1].$$

Writing down the objective function in terms of the nonlinear polarization currents, it follows that the solution of Eq. (5), obtained by employing any mathematical programming technique that makes use of gradient information, e.g., the AVM [18], maximizes the nonlinear coefficient (mode overlap) associated with the aforementioned nonlinear optical process.

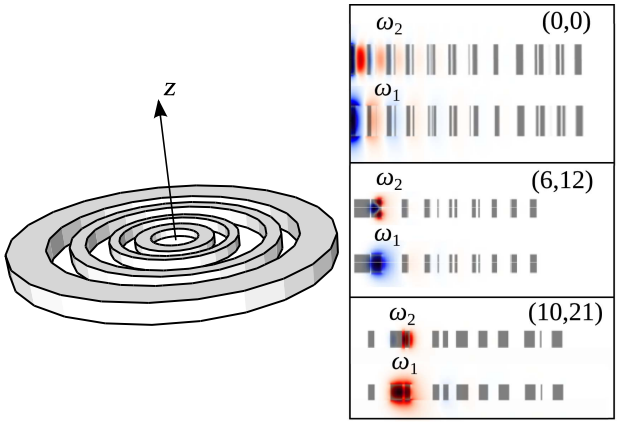

Fig. 1. Schematic illustration of topology-optimized multi-track ring resonators. Also shown are the cross-sectional profiles of several ring resonators, along with those of fundamental and second-harmonic modes corresponding to the azimuthal mode pairs (0, 0), (6, 12), and (10, 21), whose increased lifetimes and modal interactions $\tilde{\beta}$ (Table 1) via a $\chi^{(2)}$ process lead to increased SHG efficiencies.

Multi-track ring resonators. We first apply our NLTO formulation to the design of rotationally symmetric cavities for SHG. We consider a material platform consisting of gallium arsenide thin films cladded in silica. While we mainly focus on the design of unloaded cavities here, a variety of techniques can be employed to couple in and out of these cavities, including dimpled fiber tapers [22] and vertical waveguiding layers [23]. The result of the optimizations is described in Fig. 1 and Table 1, the latter of which summarizes the most important parameters, classified according to the choice of m_1 and m_2, which denote the azimuthal mode numbers of fundamental and second-harmonic modes, respectively. (Note that depending on the polarization of the two modes, different

Table 1. SHG Figures of Merit, Including Azimuthal Numbers $m_{1,2}$, Field Polarizations, Lifetimes $Q_{1,2}$, and Nonlinear Coupling $\bar{\beta}$, in Units of $\chi^{(2)}/4\sqrt{(\epsilon_0\lambda^3)}$, Corresponding to the Fundamental and Harmonic Modes of Various Topology-Optimized Multi-Track Ring Resonators, with Cross Sections (Illustrated in Fig. 1) Determined by the Choice of Thicknesses, Given in Units of λ_1

(m_1, m_2)	Polarization	Q_1	Q_2	$\bar{\beta}\left(\frac{\chi^{(2)}}{4\sqrt{(\epsilon_0\lambda^3)}}\right)$	Thickness (λ_1)
(0, 0)	(E_z, E_z)	10^5	3×10^4	0.041	0.39
(4, 8)	(E_z, E_z)	3.1×10^4	3×10^3	0.009	0.30
(5, 10)	(E_z, E_r)	8×10^3	3.7×10^4	0.008	0.18
(6, 12)	(E_z, E_z)	9.5×10^4	2.7×10^4	0.008	0.18
(10, 20)	(E_z, E_z)	10^6	1.2×10^4	0.004	0.22
(10, 21)	(E_z, E_r)	1.6×10^6	7.4×10^4	0.004	0.24

phase-matching conditions must be imposed [11,13,15], e.g., $m_2 = \{2m_1, 2m_1 \pm 1\}$, thus, in our optimizations, we consider different possible combinations.) The parameter $\bar{\beta}$ is the nonlinear coupling strength between the interacting modes, which in the case of SHG is given by [17]

$$\bar{\beta} = \frac{\int d\mathbf{r}\bar{\epsilon}(\mathbf{r})E_2^* E_1^2}{\left(\int d\mathbf{r}\epsilon_1|\mathbf{E}_1|^2\right)\left(\sqrt{\int d\mathbf{r}\epsilon_2|\mathbf{E}_2|^2}\right)}\sqrt{\lambda_1^3}. \quad (6)$$

In Table 2, we also consider resonators optimized to enhance a SFG process involving three resonant modes, $\omega_1 = \omega_3 - \omega_2$, with $\omega_2 = 1.2\omega_1$ and $\omega_3 = 2.2\omega_1$. Note that two of these modes are more than an octave apart. The definition of the corresponding nonlinear overlap factor, i.e., the generalization of Eq. (7), can be found in Refs. [15,24].

The resulting structures and figures of merit suggest the possibility of orders-of-magnitude improvements. In particular, we find that the largest overlap factors $\bar{\beta}$ are achieved in the case $m_1 = m_2 = 0$, corresponding to highly confined modes with peak amplitudes near the center of the rings [Fig. 1(a)], in which case a relatively thicker cavity $\approx 0.4\lambda_1$ is required to mitigate out-of-plane radiation losses. From the optimized Q's and $\bar{\beta}$, and assuming $\lambda_1 = 1.55$ μm, we predict a SHG efficiency of $P_2/P_1^2 = 1.3 \times 10^{25}(\chi^{(2)})^2$ [W^{-1}]. As expected, both radiative losses and $\bar{\beta}$ decrease with increasing m, as the modes become increasingly delocalized and move away from the center, resulting in larger mode volumes [Figs. 1(b) and 1(c)]. Compared to the state-of-the-art microring resonator demonstrated in Ref. [14], whose $\bar{\beta} \sim 10^{-3}$, our structures exhibit consistently larger overlaps, albeit with decreased radiative lifetimes. The main challenge in realizing multi-track designs is that, like photonic crystals and related structures that rely on careful interference effects, their Qs tend to be more sensitive to perturbations. In the case of centrally confined modes with $m_1 = m_2 = 0$, we observe the appearance of deeply subwavelength features near the cavity center where the fields are mostly confined. We find that these features are crucial to the integrity of the modes since they are responsible for the delicate interference process which cancels outgoing radiation; therefore, their absence greatly reduces the quality factors of the modes. Overall, for $m_1 = m_2 = 0$, we find that for operation with $\lambda_1 \sim 1.55$ μm, a fabrication precision of several nanometers would be necessary to ensure quality factors on the order of 10^5. On the other hand, the optimized designs become increasingly robust for larger $m_1, m_2 \gg 0$ since they have fewer subwavelength features and smaller aspect ratios. Figure 2 shows distributions of the most important figures of merit for an ensemble of ($m_1 = 6$, $m_2 = 12$) cavities subject to random, uniformly distributed structural (position and thicknesses) perturbations in the range [−50, 50] nm. We find that while the frequency mismatch and overlap factors are quite robust against variations, the quality factors can decrease to $\sim 10^4$. Although the variations simulated here respect the rotational symmetry and, thus, do not exactly correspond to experimental imperfections, they provide a theoretical measure of sensitivity of the optimized design to structural perturbations.

Slab microcavities. We now consider a different class of structure and NFC process, namely DFG in slab microcavities. In particular, we consider a $\chi^{(3)}$ nonlinear process satisfying the frequency relation $\omega_s = \omega_0 - 2\omega_b$, with ω_s, ω_0, and ω_b denoting the frequencies of signal, emitted, and pump photons, respectively (see Fig. 3). Such a DFG process has important implications for single-photon frequency conversion, e.g., in nitrogen-vacancy (NV) color centers, where a single NV photon $\lambda_0 = 637$ nm is converted to a telecommunication wavelength $\lambda_s = 1550$ nm by pump light at $\lambda_b \sim 2200$ nm, requiring resonances that are more than two octaves away from one another [25]. In other words, the challenge is to design a diamond cavity ($n \approx 2.4$) that exhibits three widely separated strongly confined modes with large nonlinear interactions and lifetimes. Figure 3 presents a proof-of-concept 2D design that satisfies all of these requirements. Extending to three-dimensional (3D) slabs of finite thickness (assuming similar lateral profiles and vertical confinement ∼ wavelength), one is led to the possibility of ultralarge $\bar{\beta} \sim 0.2$, with

$$\bar{\beta} = \frac{\int d\mathbf{r}\bar{\epsilon}(\mathbf{r})E_0^* E_b^2 E_s}{\sqrt{\int d\mathbf{r}\epsilon_0|\mathbf{E}_0|^2}\sqrt{\int d\mathbf{r}\epsilon_s|\mathbf{E}_s|^2}\left(\int d\mathbf{r}\epsilon_b|\mathbf{E}_b|^2\right)}\lambda_1^3. \quad (7)$$

Note that the lifetimes of these 2D modes are bounded only by the finite size of our computational cell (and, hence, are ignored in our discussion), whereas in realistic 3D microcavities, they will be limited by vertical radiation losses [7].

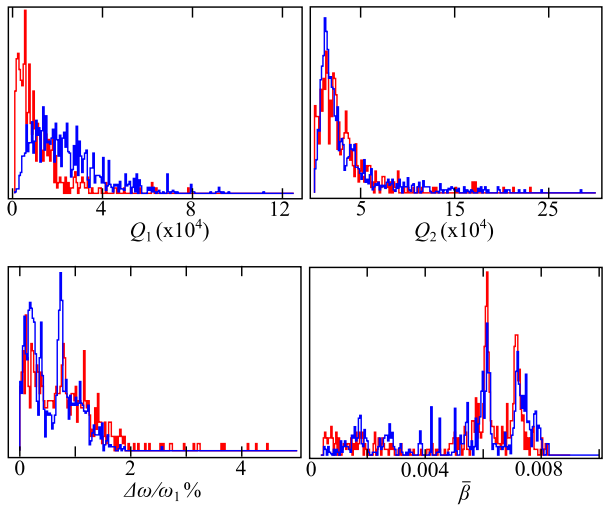

Fig. 2. Statistical distribution of lifetimes $Q_{1,2}$, frequency mismatch $\Delta\omega = |\omega_1 - \omega_2/2|$, and nonlinear coupling $\bar{\beta}$, corresponding to the multi-track ring of Fig. 1 associated with the azimuthal mode pair (6, 12). The positions of every interface are subject to random variations of maximum extent ±36 nm (blue line) or ±54 nm (red line).

Table 2. Similar Figures of Merit as in Table 1, but for Multi-Track Rings Designed to Enhance a SFG Process Involving Light at $\omega_1 = \omega_3 - \omega_2$, $\omega_2 = 1.2\omega_1$, and $\omega_3 = 2.2\omega_1$, with $\bar{\beta}$ Described in Ref. [15]

ω_1:ω_2:ω_3	(m_1, m_2, m_3)	Polarization	(Q_1, Q_2, Q_3)	$\bar{\beta}\left(\frac{\chi^{(2)}}{4\sqrt{(\epsilon_0\lambda^3)}}\right)$	Thickness (λ_1)
1:1.2:2.2	(0, 0, 0)	(E_z, E_z, E_z)	$(1.8 \times 10^4, 1.4 \times 10^4, 7800)$	0.031	0.38

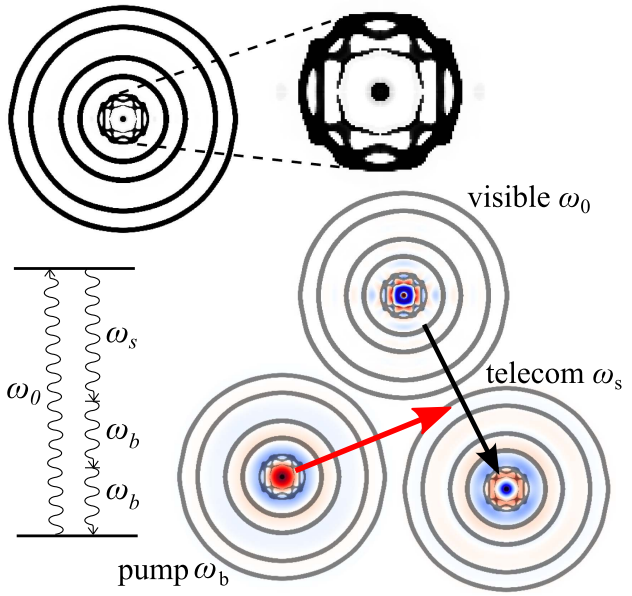

Fig. 3. Topology-optimized 2D microcavity exhibiting tightly confined and widely separated modes ($\omega_s, \omega_b, \omega_0$) that are several octaves apart. The modes interact strongly via a $\chi^{(3)}$ DFG scheme dictated by the frequency relation $\omega_s = \omega_0 - 2\omega_b$, with $\omega_0 = 2.35\omega_s$ and $\omega_b = 0.68\omega_s$, illustrated by the accompanying two-level schematic.

Despite the 2D aspect of this slab design, and in contrast to the fully 3D multi-track ring resonators above, these results provide proof of the existence of wavelength-scale photonic structures that can greatly enhance challenging NFC processes. One example is the NV problem described above, which is particularly challenging if a monolithic all-diamond approach is desired, in which case both single-photon emission and wavelength conversion are to be seamlessly realized in the same diamond cavity [25]. A viable solution that was recently proposed is the use of four-wave mixing Bragg scattering (FWM-BS) by way of whispering gallery modes [25,26], which are relatively easy to phase-match but suffer from large mode volumes. Furthermore, FWM-BS requires two pump lasers, at least one of which has a shorter wavelength than the converted signal photon, which could lead to spontaneous downconversion and undesirable noise, degrading quantum fidelity, in contrast to the DFG scheme above, based on a long-wavelength pump [25]. While the geometry given in Fig. 3 might prove challenging, we expect that an experimental realization will soon become a reality given the rapidly maturing diamond fabrication technologies [27,28].

Funding. National Science Foundation (NSF) (DGE1144152, DMR-1454836).

REFERENCES

1. K. W. DeLong, R. Trebino, J. Hunter, and W. E. White, J. Opt. Soc. Am. B **11**, 2206 (1994).
2. M. A. Arbore, A. Galvanauskas, D. Harter, M. H. Chou, and M. M. Fejer, Opt. Lett. **22**, 1341 (1997).
3. T. F. Heinz, C. K. Chen, D. Ricard, and Y. R. Shen, Phys. Rev. Lett. **48**, 478 (1982).
4. P. S. Kuo, K. L. Vodopyanov, M. M. Fejer, D. M. Simanovskii, X. Yu, J. S. Harris, D. Bliss, and D. Weyburne, Opt. Lett. **31**, 71 (2006).
5. R. Krischek, W. Wieczorek, A. Ozawa, N. Kiesel, P. Michelberger, T. Udem, and H. Weinfurter, Nat. Photonics **4**, 170 (2010).
6. S. Zaske, A. Lenhard, C. A. Keßler, J. Kettler, C. Hepp, C. Arend, R. Albrecht, W.-M. Schulz, M. Jetter, P. Michler, and C. Becher, Phys. Rev. Lett. **109**, 147404 (2012).
7. J. D. Joannopoulos, S. G. Johnson, J. N. Winn, and R. D. Meade, *Photonic Crystals: Molding the Flow of Light*, 2nd ed. (Princeton University, 2008).
8. M. Soljačić, M. Ibanescu, S. G. Johnson, Y. Fink, and J. D. Joannopoulos, Phys. Rev. E **66**, 055601(R) (2002).
9. K. Rivoire, Z. Lin, F. Hatami, W. T. Masselink, and J. Vučković, Opt. Express **17**, 22609 (2009).
10. W. H. P. Pernice, C. Xiong, C. Schuck, and H. X. Tang, Appl. Phys. Lett. **100**, 223501 (2012).
11. Z.-F. Bi, A. W. Rodriguez, H. Hashemi, D. Duchesne, M. Loncar, K.-M. Wang, and S. G. Johnson, Opt. Express **20**, 7526 (2012).
12. S. Buckley, M. Radulaski, J. L. Zhang, J. Petykiewicz, K. Biermann, and J. Vučković, Opt. Express **22**, 26498 (2014).
13. C. Wang, M. J. Burek, Z. Lin, H. A. Atikian, V. Venkataraman, I.-C. Huang, P. Stark, and M. Lončar, Opt. Express **22**, 30924 (2014).
14. X. Guo, C.-L. Zou, and H. X. Tang, Optica **3**, 1126 (2016).
15. A. Rodriguez, M. Soljačić, J. D. Joannopulos, and S. G. Johnson, Opt. Express **15**, 7303 (2007).
16. J. Bravo-Abad, A. W. Rodriguez, J. D. Joannopoulos, P. T. Rakich, S. G. Johnson, and M. Soljacic, Appl. Phys. Lett. **96**, 101110 (2010).
17. Z. Lin, X. Liang, M. Lončar, S. G. Johnson, and A. W. Rodriguez, Optica **3**, 233 (2016).
18. J. Jensen and O. Sigmund, Laser Photon. Rev. **5**, 308 (2011).
19. X. Liang and S. G. Johnson, Opt. Express **21**, 30812 (2013).
20. K. Svanberg, SIAM J. Optim. **12**, 555 (2002).
21. R. W. Boyd, *Nonlinear Optics* (Academic, 1992).
22. B. D. Hauer, P. H. Kim, C. Doolin, A. J. MacDonald, H. Ramp, and J. P. Davis, EPJ Tech. Instrum. **1**, 4 (2014).
23. N. Sherwood-Droz and M. Lipson, Opt. Express **19**, 17758 (2011).
24. I. B. Burgess, Y. Zhang, M. W. McCutcheon, A. W. Rodriguez, J. Bravo-Abad, S. G. Johnson, and M. Lončar, Opt. Express **17**, 20099 (2009).
25. Z. Lin, S. G. Johnson, A. W. Rodriguez, and M. Loncar, Opt. Express **23**, 25279 (2015).
26. Q. Li, M. Davanço, and K. Srinivasan, Nat. Photonics **10**, 406 (2016).
27. B. Hausmann, I. Bulu, V. Venkataraman, P. Deotare, and M. Lončar, Nat. Photonics **8**, 369 (2014).
28. P. Latawiec, V. Venkataraman, M. J. Burek, B. J. Hausmann, I. Bulu, and M. Lončar, Optica **2**, 924 (2015).